



Quantifying the Dislocation Cell Contribution to the Yield Strength of 316L Steel

X. He¹ · X. K. Shang¹ · B. B. He¹

Received: 25 June 2023 / Accepted: 11 September 2023 / Published online: 7 October 2023
© The Author(s) under exclusive licence to The Korean Institute of Metals and Materials 2023

Abstract

The present work investigates the contribution of dislocation cell to the yield strength of additively manufactured (AM) 316L steel through nanoindentation technique. The nano-mechanical response of the AM sample is properly compared to the heat-treated (HT) one without dislocation cell. The nanoindentation size effect is observed in both samples. Although the nanohardness of HT sample is comparable to that of AM sample at low indentation depth, the former is obviously lower than the later at depth where the indentation impression is similar or larger than that of dislocation cell. Utilizing Nix–Gao model and Tabor equation, the contribution of dislocation cell to the yield strength is estimated to be ~ 169 MPa, which is about 54% of the improved yield strength.

Keywords Dislocation cell · GND · Additive manufacturing · Nanoindentation

1 Introduction

Metal additive manufacturing (AM) enables unique building strategy in a disruptive way, allowing the large freedom of designing sophisticated components in a short duration [1]. The metallic material is subjected to a complex thermal history during AM process, including rapid solidification and repeated heating/cooling, which results in extremely nonequilibrium microstructures and metastable phases [2]. Typically, hierarchically heterogeneous microstructures including coarse grains, solidification textures, fine elongated cells, and nanoscale inclusions are usually found in the AM metallic materials such as the typical 316L [3]. The AM 316L exhibits excellent mechanical properties owing to the complex hierarchical microstructures across different length scales [3–6]. The strengthening effect of the dislocation cell structure in AM 316L has been intensively discussed [3, 7–11]. It has reported that the strengthening effect of the cell boundary (CB) can be related to the Hall–Petch relation, which is similar to the grain boundary (GB) strengthening [3, 7]. However, the CB cannot simply be compared to the

GB owing to the low misorientation angles between adjacent cells [9] and that the GB is a stronger barrier for the glide of dislocation than the CB [10, 12, 13]. It has been shown that the cell spacing scale with the strength of AM 316L [14]. Nevertheless, it is impossible to construct a single size scaling equation for cell structures due to the nonuniform cell size with average spacing ranging from 0.2 to 1 μm and varying from region to region within the same sample [15]. The nonuniform distribution of the cell size is suggested to be correlated with the building geometry and laser parameters [16]. Additionally, the misorientations across most CBs cannot be revealed by EBSD IPF orientation mapping, suggesting that the cell walls should be treated differently from traditional interfaces such as dislocation walls or high angle grain boundaries (HAGBs) [3]. Therefore, the strengthening effect of the cell structures is not well understood and the contribution of CB strengthening to the macroscopic strength remains to be studied.

Nanoindentation is a reliable technique to measure local mechanical properties such as elastic modulus and hardness [17, 18]. Nanoindentation tests has been already used to analyzed the scale-dependent plasticity properties [19–21], activated slip systems [22], and yield strength [23, 24]. The indentation size effect (ISE) is an important aspect of nanoindentation, which depicts the relation between hardness and penetration depth, i.e., the increase in penetration depth results in a decrease in indentation hardness [25, 26].

✉ B. B. He
hebb@sustech.edu.cn

¹ Department of Mechanical and Energy Engineering,
Southern University of Science and Technology,
Shenzhen 518055, China

This phenomenon can be explained by the deformation-induced strain gradients which induce geometrically necessary dislocations (GNDs) [25]. The variation of indentation hardness has been explored as a function of penetration depth [27].

In this contribution, we are aimed to reveal the strengthening contribution of the dislocation cell structure to the macroscopic strength of AM 316L via nanoindentation technique. By comparing to the heat-treated (HT) 316L sample, the increment of the nanohardness of AM 316L sample can be uniquely determined. However, owing to the presence of ISE and the change of deformation mechanisms under different penetration depth, we employed the intercept of the linear fitting to the nanohardness at different depths according to the classic Nix–Gao model [25]. Consequently, the contribution of the CB strengthening to the yield strength of AM steel is determined.

2 Experiments

The 316L stainless steel (Fe–18Cr–13Ni–2.3Mo–0.8Mn–0.7Si) samples used in the present investigation are fabricated via the laser powder bed fusion technique (DiMetal-100 H, 200 W, 40 μm beam diameter). The laser power, scan rate, hatch spacing, and layer thickness are 200 W, 283 mm/s, 300 μm , and 30 μm , respectively. The rotational scanning with the angle between each layer of 67° is selected to obtain a relatively isotropic mechanical property [28]. For comparison purpose, the AM 316L sample is heat treated at 1200 $^\circ\text{C}$ for 1 h to obtain a fully recrystallized microstructure [29], which is termed as HT sample hereafter. The samples for microstructure characterization and nanoindentation tests are prepared through the electropolishing technique in a solution of 10% perchloric acid and 90% ethanol (vol%) at room temperature. The nanoindentation measurement is conducted on the top surface normal to the build direction using an iNano nanoindenter (KLA, Inc.) with a Berkovich indenter with a half angle of 65.3° in a load-controlled mode at room temperature. Prior to the nanoindentation test, a tip-area calibration was performed on a fused silica sample for tip radius verification. Ten peak loads (P_{max}) ranging from 0.5 mN to 10 mN are applied with the loading part finished in 10 s and holding segment at the peak load for 1 s. Each peak load consists of one indentation matrix with 2×10 points and a spacing of 20 μm to avoid the interference among the adjacent indents. The initial microstructure and position of indents are captured by the scanning electron microscope (SEM, Merlin, ZEISS) equipped with an electron backscatter diffraction detector (EBSD, Digiview4, EDAX Inc.). For EBSD data collection, the accelerating voltage of 20 kV, current of 5 nA, and step size of 2 μm are used. The microstructural evolution underneath the indents is observed by

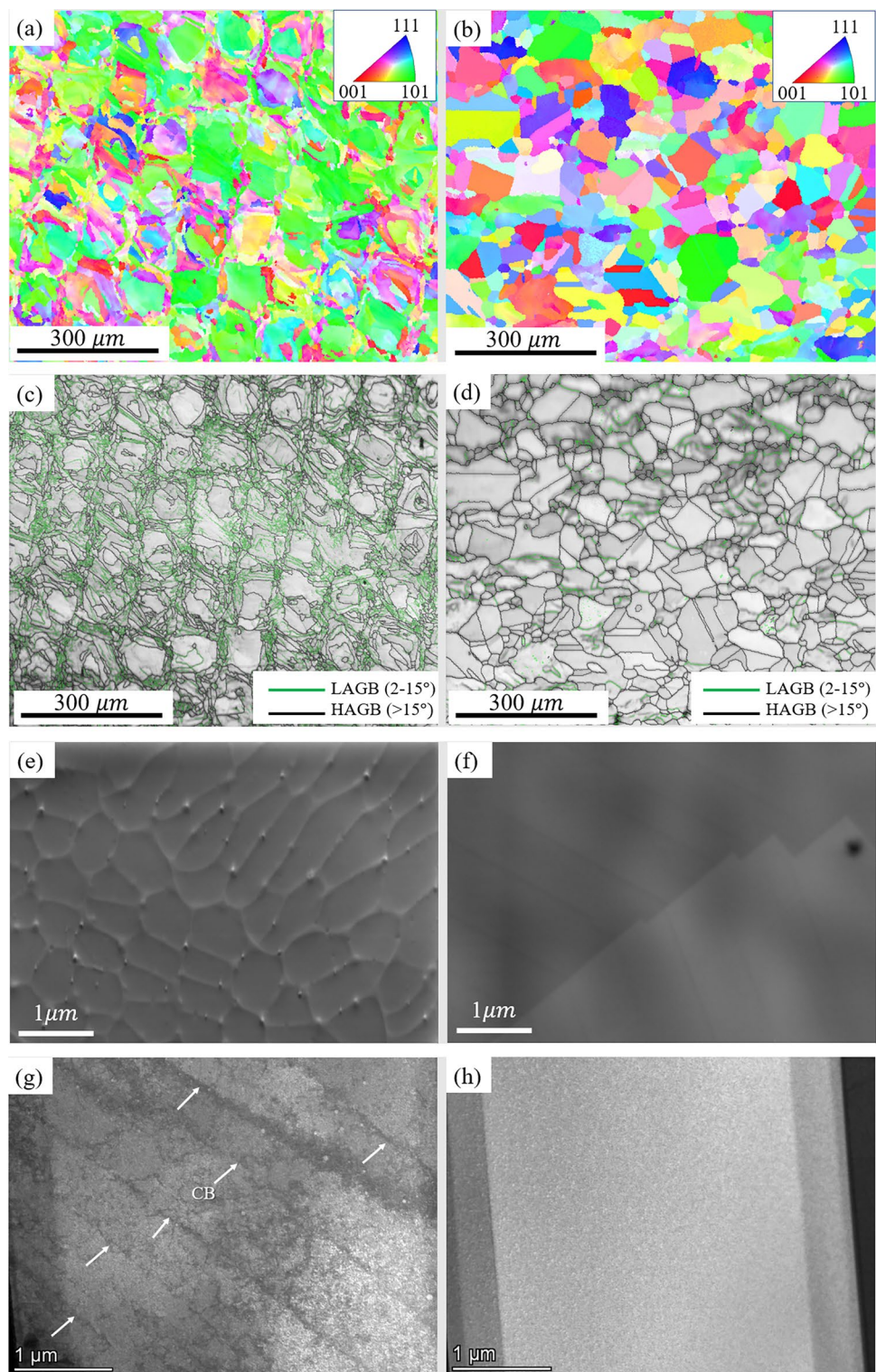
transmission electron microscopy (TEM, Talos F200X G2, Thermo Fisher). The specimens for TEM observation are prepared by focused ion beam milling (FIB, Helios 600i, FEI). The macroscopic mechanical properties of the AM and HT 316L are characterized by tensile test. The dog-bone tensile specimens with a gauge dimension of $10 \times 4 \times 2.5 \text{ mm}^3$ are extracted from the AM 316L blocks perpendicular to the BD using wire electrical discharge machining. The tensile tests are performed using a universal tensile testing machine with a strain rate of 10^{-3} s^{-1} under room temperature.

3 Results

The AM sample shows a strong anisotropic microstructure, with the $\langle 110 \rangle$ -texture tending to align along the BD (Fig. 1a). The grains of the AM sample exhibit a Mosaic-type pattern and the grain size is heterogeneous and with an average diameter of $\sim 13 \mu\text{m}$ (Fig. 1a). In contrast, after the heat treatment at 1200 $^\circ\text{C}$ for 1 h, the HT sample demonstrates a fully recrystallized microstructure (Fig. 1b). The Mosaic-type pattern all disappeared, and with an almost random texture and a slightly increased average grain size of $\sim 26 \mu\text{m}$ (Fig. 1b). Interestingly, the band contrast map shows a high density of low-angle grain boundaries (LAGBs) in the AM sample as shown in Fig. 1c, which is sharply different from the HT sample with significantly decreased amount of LAGB (Fig. 1d). The SEM image confirms the formation of dislocation cell structure in the AM sample (Fig. 1e). These dislocation cells could be responsible for the presence of LAGB in the EBSD band contrast map (Fig. 1c). However, only ledge of grain boundary is identified in the HT sample without formation of dislocation cells based on the SEM observation (Fig. 1f). The dislocation cells in the AM sample are characterized by high-density dislocations enriched at the CBs as shown in the cross-section STEM image (Fig. 1g). In contrast, no dislocation cells are found in the HT sample based on the TEM observation (Fig. 1h). Thus, two samples with sharply different substructures can be obtained, which is confirmed by the detailed microstructural observation (Fig. 1).

The position of indents is identified by the SEM observation. The indents that are close to the grain boundaries are disregarded for data analysis. The typical morphology of indents with peak load (P_{max}) of 0.5 and 8 mN on the AM sample is shown in Fig. 2. The indentation size with a P_{max} of 1 mN on the AM sample is $\sim 450 \text{ nm}$, which is similar to the cell size ($\sim 500 \text{ nm}$). With increase of the P_{max} , the size of indentation impression increased correspondingly. For instance, the side of indents under the maximum load of 8 mN can cover about five dislocation cells. No obvious pile-up or sink-in is observed in the free surface surrounding the indentation impressions in the AM sample (Fig. 2).

Fig. 1 The EBSD IPF image of **a** AM and **b** HT samples. The band contrast map showing the distribution of grain boundaries in **c** AM and **d** HT samples. The green line represents the low angle grain boundary (LAGB, 2° – 15°) while the black line indicates the high angle grain boundary (HAGB, $> 15^{\circ}$). **e** SEM image of AM sample showing the distribution of dislocation cell structures. **f** SEM image of HT sample showing the ledge of grain boundary without the presence of dislocation cells. **g** STEM image demonstrating the formation of cell boundaries (CB) in the AM sample. **h** STEM image demonstrating the absence of dislocations in the HT sample. (For interpretation of the references to color in this figure legend, the reader is referred to the web version of this article)



The indents on the HT sample are also observed by SEM as shown in Fig. 3. Different from the indents of AM sample, many slip traces adjacent to the indentation impressions are found in almost all tests with different P_{max} (Fig. 3). In particular, the slip traces along two different directions are

observed on one side of indents under the maximum load of 1 mN and 8 mN. The formation of slip traces at the free surface could be the intersection of the sample surface and the $\{111\}\langle 110 \rangle$ slip systems of the HT 316L with a face-centered cubic (FCC) lattice structure [30].

Fig. 2 SEM images showing the typical indentation impressions with P_{max} of 1 mN and 8 mN on the AM sample

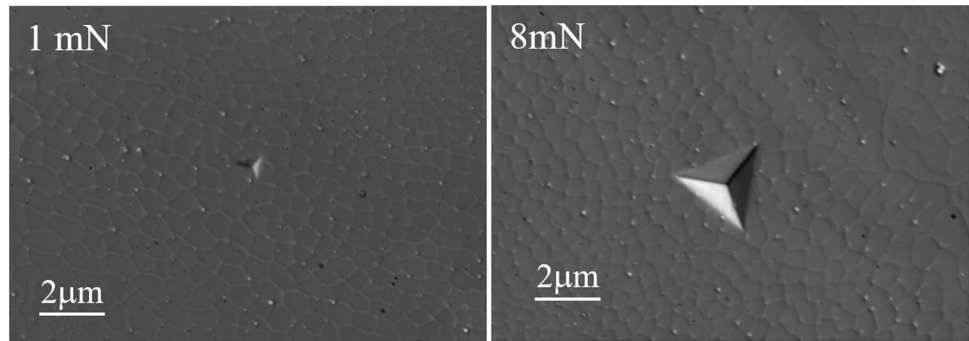


Fig. 3 SEM images showing the typical indentation impressions with P_{max} of 1 mN and 8 mN on the HT sample. The slip traces can be observed on the free surface close to the indentation impressions

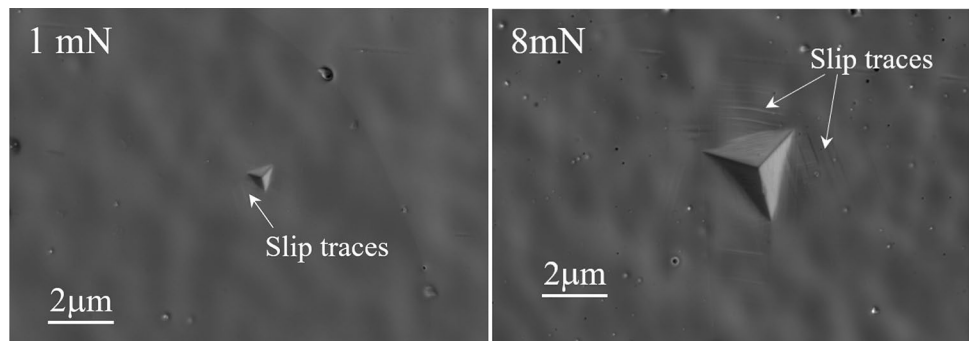


Figure 4a, b shows the typical P – h curves with different P_{max} on the AM and HT samples, respectively. In general, the maximum depth at the large peak load for AM sample is lower than that for HT sample (Fig. 4a, b). However, for the small peak load, the maximum depth for AM sample is even slightly larger than that for HT sample (Fig. 4a, b). This point can be vividly captured by plotting the 1 mN P – h curve of the AM and HT samples as shown in Fig. 4c. The Hertzian solution for elastic contact of nanoindentation tests reads [31]:

$$P = \frac{4}{3} E_r R_i^{\frac{1}{2}} h^{\frac{3}{2}} \quad (1)$$

$$\frac{1}{E_r} = \frac{1 - \nu_i^2}{E_i} + \frac{1 - \nu_s^2}{E_s} \quad (2)$$

where $R_i = 50$ nm is the indenter tip radius verified from the prior calibration according to literature [32], P is the indentation load, h is the penetration depth of indentation, E_r is the reduced modulus, E and ν are Young's modulus and Poisson's ratio, and the subscripts s and i represent the sample and indenter, respectively. The Hertzian fitting is calculated from Eq. (1), with E and ν for the specimen and indenter of 187 GPa and 0.3 [33], 1140 GPa and 0.07 [34], respectively. The P – h curve departs from the Hertzian solution at the pop-in with a depth of ~ 12 nm in HT sample (Fig. 4c). In contrast, no obvious pop-in is observed for the

AM sample. The maximum shear stress (i.e., pop-in stress) τ_{max} for the elastic regime is given as [31, 35]:

$$\tau_{max} = \frac{0.31}{\pi} \left(\frac{6PE_r^2}{R_i^2} \right)^{1/3} \quad (3)$$

Taking the pop-in load for the HT 316L as 61 μ N, the maximum shear stresses are calculated to be 16.2 GPa, which is comparable to the ideal shear stress ($E/10$) and is thus large enough to nucleate the dislocations beneath the indenter. The absence of pop-in event for AM sample could be due to the presence of intensive dislocations in the AM sample as shown in Fig. 1g so that the indentation tip (~ 50 nm) can easily indent on individual dislocations so that the nucleation of dislocations is not necessary in this process. For the same reason, the rather low dislocation density in the HT sample (Fig. 1h) requires the nucleation of dislocations to initiate the plasticity during indentation process.

Figure 4c also gives the GND fitting of the 1 mN P – h curves of AM and HT samples according to the following Eqs. [25, 35, 36]:

$$P = A_c MC \beta G b \sqrt{\rho_{SSD} + \rho_{GND}} \quad (4)$$

$$\rho_{GND} = \frac{3}{2} \frac{1}{f^3} \frac{\tan^2 \theta}{bh} \quad (5)$$

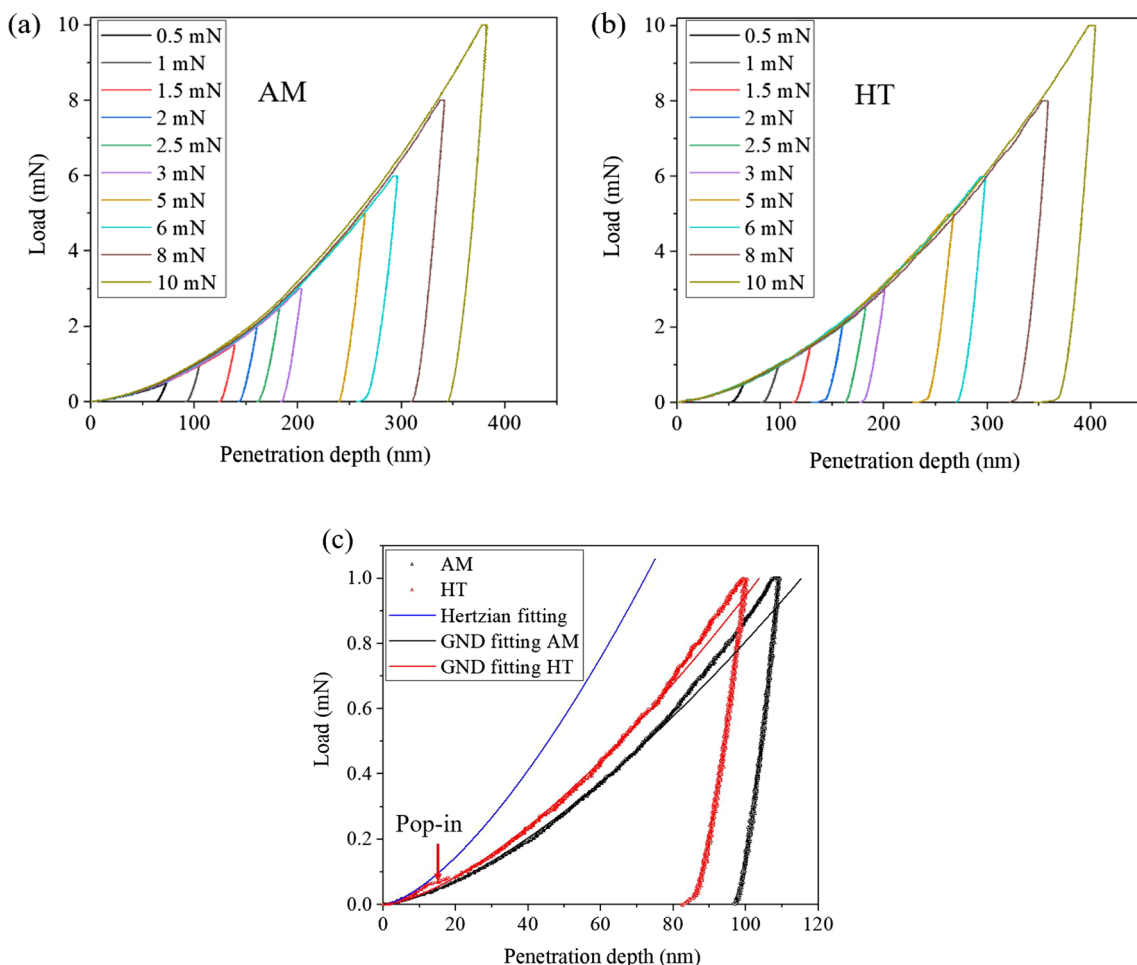


Fig. 4 The P – h curves with different P_{max} on the **a** AM and **b** HT samples, **c** the P – h curve with peak load of 1 mN of AM and HT samples. The blue, red, and black lines are the fitting curves of the Hertzian elastic contact solution, the GND concept of AM and HT

sample, respectively (For interpretation of the references to color in this figure legend, the reader is referred to the web version of this article)

where $A_c = 24.5h^2$ is the first approximation of projected contact area for the ideal Berkovich indenter, $M = 3$ is the Taylor factor, $C = 3$ is the constraint factor, $\beta = 0.5$ represents the dislocation structure, $G = 72$ GPa is the shear modulus, and $b = 0.254$ nm is the Burgers vector for 316L, $\tan\theta = 0.358$ is the geometrical factor for Berkovich indenter, ρ_{SSD} and ρ_{GND} are the statistically stored dislocation (SSD) and GND density in the plastic zone, but the ρ_{SSD} is omitted here due to the small indentation depth [37], and f is the ratio of the plastic zone radius a_{pz} to the contact radius a_c . When ignoring the ρ_{SSD} , $f = 1.98$ and 1.78 gives the best fitting to the P – h curves at $h < 70$ nm of AM and HT sample, respectively. The higher f value means a larger plastic zone and lower ρ_{GND} of the AM sample than that of the HT sample. The deviation of the GND fitting to the P – h curve with higher indentation depth (> 70 nm) in both AM and HT samples could be ascribed to the non-negligible role of the SSD in plastic deformation.

Figure 5a plots the nanohardness of AM and HT samples at different penetration depths. It is shown that both nanohardness of the AM and HT samples decreases rapidly at the low penetration depth in the range of 100–150 nm, and then decreases slowly with increase of the penetration depth. The nanohardness of the HT sample is slightly higher than that of the AM sample when the penetration depth is below ~ 100 nm, but when surpasses this depth, the condition reverses (Fig. 5a). This indicates a transition of deformation mechanism during nanoindentation. The typical indentation size effect (ISE) [38–41] which manifests the nanohardness decrease with an increase in the penetration depth ($< 1 \mu\text{m}$) is observed for both samples. The ISE can be calculated by using the GND concept based on the Nix–Gao model [25] as,

$$H = H_0 \sqrt{1 + h^*/h} \tag{6}$$

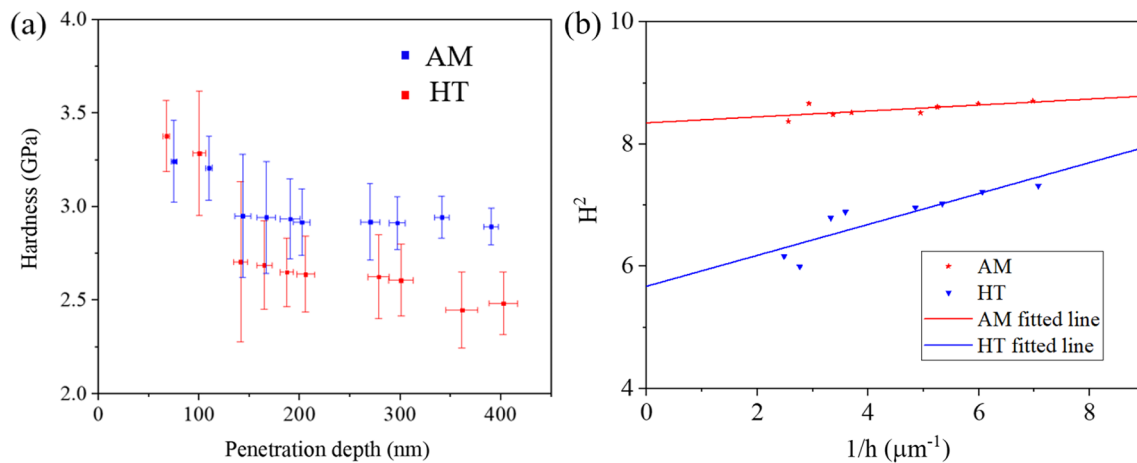


Fig. 5 **a** The plot of nanohardness against indentation penetration depth for AM and HT samples. **b** The linear fitting of the experimental data by using GND concept developed by Nix–Gao [25]. (Color figure online)

where H is the hardness that corresponds to a specific penetration depth h . H_0 is the constant hardness value obtained at an infinite depth and h^* is the characteristic depth depending on the hardness [25, 42]. Equation (6) can be rewritten as,

$$H^2 = H_0^2(1 + h^*/h) \quad (7)$$

where H and h can be obtained from indentation experiments. Then, both H_0 and h^* can be fitted out by using Eq. (7). Figure 5b depicts the correlation of H_0 and $1/h$ for the AM and HT samples based on the Nix–Gao model. Note that, the Nix–Gao model that is based on Taylor hardening [25], thus the dislocation nucleation mediated plasticity indentation data (i.e., 0.5 and 1 mN) are excluded in the fitting (Fig. 5b). In the present study, the H_0 and h^* are figured out to be 2.889 GPa, 48.7 nm for the AM sample and 2.382 GPa, 252.8 nm for the HT sample, respectively.

4 Discussion

The pop-in behavior in nanoindentation test is related to the onset of plasticity [36, 43, 44]. The initial loading is essentially elastic and can be modeled using Hertzian contact theory as shown in Fig. 4c [31]. Before the pop-in event, a large amount of elastic energy is generated by plastic strain and stored because of the lack of mobile defects to release it. Thus, upon catastrophic plasticity (i.e., pop-in), a high density of dislocations is formed under the indenter [45], via either homogeneous [46, 47] or heterogeneous nucleation from the immobile defects [48, 49] triggers the release of the stored elastic energy [50]. In our experiment, the pop-in occurs for the HT sample while it is absent for the AM sample. Due to nearly free of dislocation in the HT sample (Fig. 1h), the onset of plasticity is believed to be associated

with homogeneous nucleation of dislocation under high indentation stress. However, the pre-existed high-density dislocations in the AM sample (Fig. 1g) can help release the stored elastic energy and facilitate the heterogeneous nucleation of dislocation with much lower indentation stress, enabling the continuous plastic deformation in AM sample (Fig. 4c).

Right after the pop-in at a relatively small indentation depth h of ~ 15 nm (Fig. 4c), the homogeneously nucleated dislocations in the HT sample serve as the nuclei for heterogeneous dislocation nucleation, which largely decreases the shear stress for dislocation nucleation [51, 52]. Thus, the resistance of deformation estimated from the stress at pop-in which is based on dislocation nucleation is changed to the shear stress governed by the Taylor dislocation model. However, the number of heterogeneous nuclei in the HT sample determined by the homogeneous dislocation nucleation is markedly lower than that of the AM sample that introduced by AM process. Consequently, the plastic deformation of the HT sample lags to the AM sample, with a smaller h and higher ρ_{GND} which in return further increases the resistance to deformation, i.e., higher hardness. Thus, the plastic deformation in this stage is mainly mediated by nucleation of dislocation.

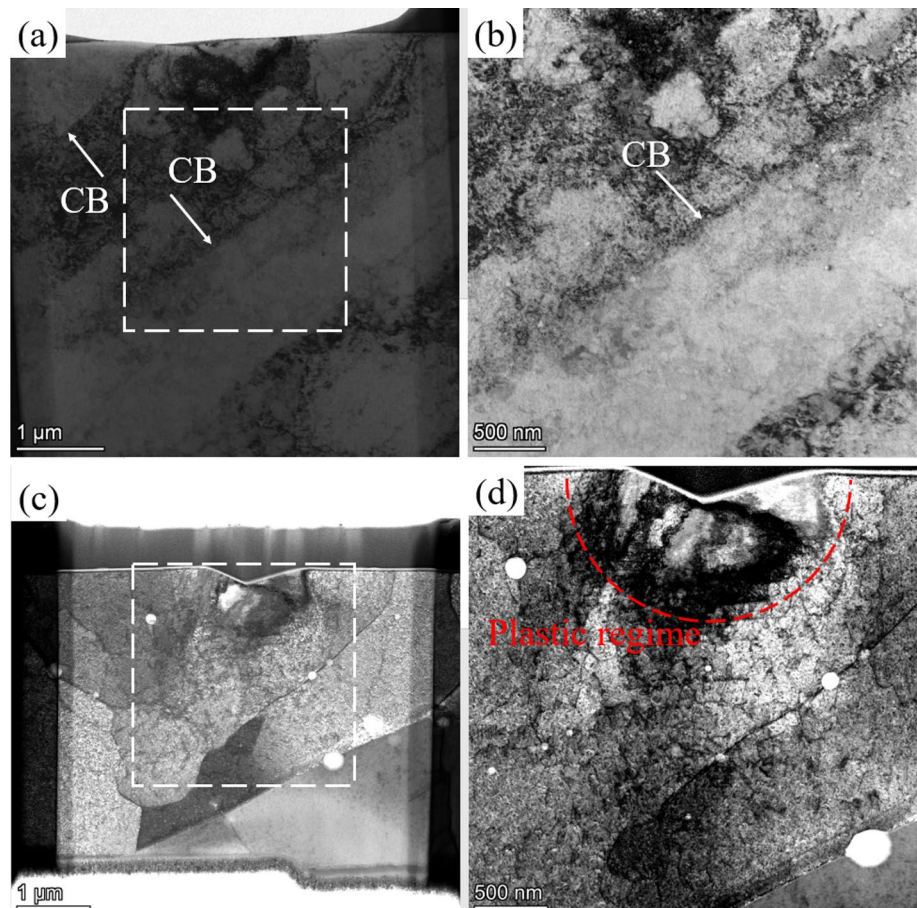
When the indentation depth is in a larger range ($h > 150$ nm) (Fig. 5a), the dominant plastic deformation mechanism transits from dislocation nucleation to motion of dislocation. In this stage, the dislocations can slip easily in the HT sample, due to the lack of obstructions from the pre-existed dislocations, and some dislocations slip to the free surface, leaving the slip traces on the free surface near the indentation (Fig. 3). The slip traces are suggested to be the intersection of the sample surface and the {111} slip planes of the individual grain with an FCC lattice structure [30], which indicates that glide of dislocation is one of the

main plastic deformation mechanisms for nanoindentation at room temperature [53, 54]. The slip traces adjacent to the indentation is a characteristic of polycrystals or other materials deforming via conventional homogeneous plasticity [55]. During the indentation test, the local plastic deformation led to generation of intensive dislocations and transmitted away from the indentation. In the case of the HT sample, there is nearly free of dislocation (Fig. 1h) to impede the dislocation motion within a relatively large grain. Consequently, the dislocations generated during nanoindentation can easily slip on the $\{111\}\langle 110\rangle$ slip systems and leave the slip traces away on the top surface. However, in the AM sample, the pre-existed dislocation cell structure (Fig. 1g) is an effective obstruction for dislocation motion, the slip of dislocation is confined, thus no slip traces are observed on the sample surface. In other words, the absence of slip traces for indentations in AM sample can be ascribed to the interaction of dislocation generated under nanoindentation with the pre-existed dislocation cell structure of the AM sample. Additionally, the nanohardness of the AM sample in the relatively large penetration depth is higher than that of HT sample, which indicating that the main factor for the larger H_0 of the AM sample (H_0^{AM}) is a result of the interaction between

the dislocation generated under nanoindentation and the dislocation cell structure.

The indentation generates complex stresses and strains fields adjacent to the indenter [56], which would produce an approximately hemispherical deformed regime right under the indenter tip [57, 58]. In the present study, the high-density dislocations concentrated within the indentation plastic zone of indents under the peak load of 5 mN are observed in both AM and HT samples (Fig. 6). These dislocations can be viewed as GNDs to accommodate the plastic deformation of the indentation [25]. In the case of the AM sample, the indentation is located right in an individual dislocation cell interior (Fig. 6a, b). It seems that these dislocations are confined in the cell interior by the CBs, as they can freely transmit along the lateral direction under the indentation stress but are not able to across the CBs. It is well known that the dislocation cell structure can effectively “modulate” the dislocation motion [59, 60], thus the dislocation generated upon local deformation of indentation can be obstructed, absorbed, or annihilated by interaction with the dislocation cell structure, thus upon these actions, the penetration of the indenter into the AM sample is largely hindered under the same maximum load as compared to the HT sample. In the HT sample, the recrystallized microstructure is nearly free

Fig. 6 **a** STEM image of the cross-section of the indent under peak load of 5 mN for AM sample. **b** The enlarged view of dashed rectangle in **a**, showing the intensive dislocations in the indentation plastic zone. **c** STEM image of the cross-section of the indent under peak load of 5 mN for HT sample. **d** The magnified view of dashed rectangle in **c**, demonstrating the distribution of dislocations in the deformation plastic zone in HT sample



of dislocation (Fig. 1h), thus the dislocation nucleation site could be at the region close to the indenter tip rather than other external sources. Moreover, due to the lack of obstructions, the dislocation generated under the indentation stress can transmit equivalently in all slip directions, as denoted in Fig. 6d.

The AM sample exhibits a high yield strength of 550 MPa based on 0.2% proof stress according to the uniaxial tensile test (Fig. 7). The yield stress of AM sample is much larger than that of the HT sample (235 MPa), which can be ascribed to the strengthening effect of sub-structures, i.e., HAGBs, LAGBs, dislocation cell structure, etc. [3, 61]. Considering the small deformation volume of the nanoindentation in the present study (below several microns), the difference of nanohardness between the AM and HT samples ($\Delta H_0 = H_0^{AM} - H_0^{HT}$) can be derived from the different strengthening effect of the dislocation cell structure [13]. Based on the Nix–Gao model, we can obtain the constant hardness value at an infinite depth, that is the intercept of the linear fitting to the y-axis in Fig. 5b. Note the Tabor equation ($\Delta\sigma = \Delta H_0/3$) is frequently employed to estimate the flow stress based on the hardness, especially useful for materials that are hardly or even unavailable to acquire the flow stress [62]. Note that in some studies, the parameter of 4.4 is selected in the Tabor equation to consider the small indentation volume at shallow indentation depth [63]. However, it is obvious that the indentation size effect together with the change of the deformation mechanism at different penetration depth affect the difference of the hardness between the AM and HT samples. Since the obtained value of the H_0 represents the hardness at an infinite depth, the conventional Tabor equation with a parameter of 3 can be used in the present study. According to the Tabor equation

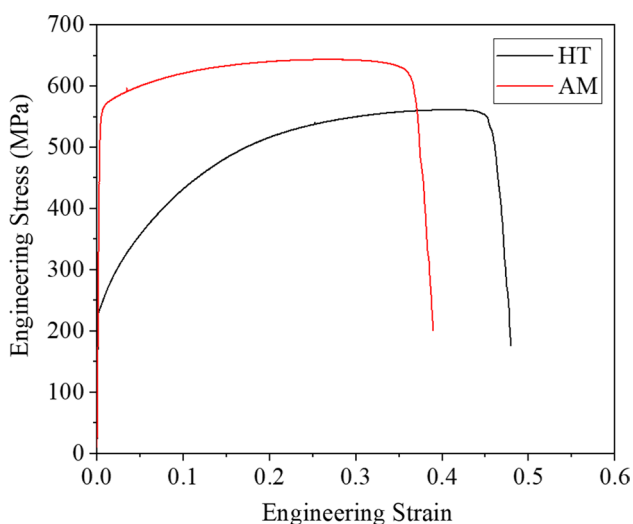


Fig. 7 The engineering stress–strain curve of the AM and HT samples. (Color figure online)

($\Delta\sigma = \Delta H_0/3$), the calculated strength increment caused by the dislocation cell structure is ~ 169 MPa, which is $\sim 54\%$ of the total increment of tensile yield strength (315 MPa). The other strengthening defects such as grain boundaries may contribute to the rest of the increased yield strength.

The present work provides a quantitative estimation on the strengthening effect of the dislocation cell structure on the macroscopic tensile yield strength based on the detailed nanoindentation investigation. The standard deviation of the nanohardness to the mean value as indicated by the error bar of nanohardness in Fig. 5a is relatively large. Several possible microstructural features including the surface roughness and the presence of nanoparticles could affect the nanohardness. Nevertheless, other effects such as grain boundary on the nanohardness are avoided by disregarding the indents that are close to the grain boundaries. The effect of crystal orientation on nanohardness is minimized by performing 20 indentations with spacing of 20 μm so that the different orientations can be incorporated in the mean value of each nanohardness. Thus, the data presented in Fig. 5a is statistical sound and can be used to reliably estimate the contribution of the dislocation cell structure to the increment of tensile yield strength. In future, the in-situ nanoindentation techniques assisted by the observation under the SEM-EBSD can precisely capture the effect of individual dislocation cell structure on the nano-mechanical behavior of the AM sample.

5 Conclusion

The present study reveals the strengthening effect of the dislocation cell structure in the AM 316L by nanoindentation technique, which is assisted by detailed microstructural observation using EBSD and TEM. The formation of slip traces, pop-in behavior, and deformation mechanisms are associated with the dislocation cell structure. The strengthening contribution of the dislocation cell structure to the yield strength of AM 316L is derived through the Nix–Gao model and Tabor equation. The conclusions are drawn as below.

1. Many slip traces adjacent to the indentation are found in the HT sample, which indicates the glide of dislocations is one of the main plastic deformation mechanisms for nanoindentation at room temperature. In contrast, the indentation impression on the AM sample is free of slip traces, suggesting that the dislocation cell structure can effectively impeded the motion of dislocation to the surface.
2. Obvious pop-in is observed in the HT sample while it is absent in the AM sample, which can be explained by the different dislocation nucleation mechanism in

AM (heterogeneous nucleation) and HT (homogeneous nucleation) samples.

3. The nanohardness of the AM sample is slightly lower than that of the HT sample at small penetration depth (~ 100 nm). When penetration depth in a relatively large range (> 150 nm), the nanohardness of the AM sample is higher than that of the HT sample, and both decrease relatively slowly, which indicates a transition of deformation mechanism from the dislocation nucleation mediated plasticity to the glide of dislocation.
4. The strengthening effect of dislocation cell structure is calculated to be ~ 169 MPa from the nanohardness data by using the Nix–Gao model and Tabor equation, which is ~ 54% of the total increment of tensile strength (315 MPa).

Supplementary Information The online version contains supplementary material available at <https://doi.org/10.1007/s12540-023-01539-y>.

Acknowledgements B.B. He gratefully acknowledges the financial support from the National Natural Science Foundation of China (Grant No. U52071173) and Science and Technology Innovation Commission of Shenzhen (Project Nos. JCYJ20210324120209026; KQTD2019092917250571) and Major Talent Programs of Guangdong Province (Contract No. 2019QN01C435). The authors would like to acknowledge the technical support from SUSTech Core Research Facilities.

Data Availability The raw data required to reproduce these findings are available from the corresponding author of this paper. The processed data required to reproduce these findings are available from the corresponding author of this paper.

Declarations

Conflict of interest On behalf of all authors, the corresponding authors state that there is no conflict of interest.

References

1. S.H. Huang, P. Liu, A. Mokasdar, L. Hou, *Int. J. Adv. Manuf. Technol.* **67**, 1191–1203 (2012)
2. D. Herzog, V. Seyda, E. Wycisk, C. Emmelmann, *Acta Mater.* **117**, 371–392 (2016)
3. Y.M. Wang, T. Voisin, J.T. McKeown, J. Ye, N.P. Calta, Z. Li, Z. Zeng, Y. Zhang, W. Chen, T.T. Roehling, R.T. Ott, M.K. Santala, P.J. Depond, M.J. Matthews, A.V. Hamza, T. Zhu, *Nat. Mater.* **17**, 63–71 (2017)
4. X. Wang, J.A. Muñoz-Lerma, O. Sanchez-Mata, M. Attarian Shandiz, N. Brodusch, R. Gauvin, M. Brochu, *Scr. Mater.* **163**, 51–56 (2019)
5. X. Wang, J.A. Muñoz-Lerma, M. Attarian Shandiz, O. Sanchez-Mata, M. Brochu, *Mater. Sci. Eng. A* **766**, 138395 (2019)
6. M. Shamsujjoha, S.R. Agnew, J.M. Fitz-Gerald, W.R. Moore, T.A. Newman, *Metall. Mater. Trans. A* **49**, 3011–3027 (2018)
7. P. Krakhmalev, G. Fredriksson, K. Svensson, I. Yadroitsev, I. Yadroitsava, M. Thuvander, R. Peng, *Metals-Basel*. **8**, 643 (2018)
8. C. Qiu, M.A. Kindi, A.S. Aladawi, I.A. Hatmi, *Sci. Rep.* **8**, 7785 (2018)
9. P. Köhnen, M. Létang, M. Voshage, J.H. Schleifenbaum, C. Haase, *Addit. Manuf.* **30**, 100914 (2019)
10. D. Kong, C. Dong, X. Ni, L. Zhang, X. Li, *Mater. Lett.* **279**, 128524 (2020)
11. T. Pinomaa, M. Lindroos, M. Walbrühl, N. Provatas, A. Laukkanen, *Acta Mater.* **184**, 1–16 (2020)
12. D. Kong, C. Dong, X. Ni, Z. Liang, C. Man, X. Li, *Mater. Res. Lett.* **8**, 390–397 (2020)
13. A.J. Birnbaum, H. Ryou, J.C. Steuben, A.P. Iliopoulos, K.J. Wahl, J.G. Michopoulos, *Mater. Lett.* **280**, 128570 (2020)
14. Y. Zhong, L. Liu, S. Wikman, D. Cui, Z. Shen, *J. Nucl. Mater.* **470**, 170–178 (2016)
15. J.R. Trelewicz, G.P. Halada, O.K. Donaldson, G. Manogharan, *Jom* **68**, 850–859 (2016)
16. Z. Li, T. Voisin, J.T. McKeown, J.C. Ye, T. Braun, C. Kamath, W.E. King, Y.M. Wang, *Int. J. Plast.* **120**, 395–410 (2019)
17. J. Marsh, Y.S. Han, D. Verma, V. Tomar, *Int. J. Plast.* **74**, 127–140 (2015)
18. H. Wang, A. Dhiman, H.E. Ostergaard, Y. Zhang, T. Siegmund, J.J. Kruzic, V. Tomar, *Int. J. Plast.* **120**, 380–394 (2019)
19. C.F.O. Dahlberg, Y. Saito, M.S. Öztop, J.W. Kysar, *Int. J. Plast.* **54**, 81–95 (2014)
20. E. Renner, Y. Gaillard, F. Richard, F. Amiot, P. Delobelle, *Int. J. Plast.* **77**, 118–140 (2016)
21. S. Xu, R. Che, L. Xiong, Y. Chen, D.L. McDowell, *Int. J. Plast.* **72**, 91–126 (2015)
22. P.A. Sabnis, S. Forest, N.K. Arakere, V.A. Yastrebov, *Int. J. Plast.* **51**, 200–217 (2013)
23. S.-K. Kang, Y.-C. Kim, K.-H. Kim, J.-Y. Kim, D. Kwon, *Int. J. Plast.* **49**, 1–15 (2013)
24. S.J. Vachhani, R.D. Doherty, S.R. Kalidindi, *Int. J. Plast.* **81**, 87–101 (2016)
25. W.D. Nix, H.J. Gao, *J. Mech. Phys. Solids*. **46**, 411–425 (1998)
26. N.A. Fleck, G.M. Muller, M.F. Ashby, J.W. Hutchinson, *Acta Metall. Mater.* **42**, 475–487 (1994)
27. N.A. Stelmashenko, M.G. Walls, L.M. Brown, Y.V. Milman, *Acta Metall. Mater.* **41**, 2855–2865 (1993)
28. L. Cui, S. Jiang, J. Xu, R.L. Peng, R.T. Mousavian, J. Moverare, *Mater. Design* **198**, 109385 (2021)
29. T. Voisin, J.-B. Forien, A. Perron, S. Aubry, N. Bertin, A. Samanta, A. Baker, Y.M. Wang, *Acta Mater.* **203**, 116476 (2021)
30. S. Tekumalla, B. Selvarajou, S. Raman, S.B. Gao, M. Seita, *Mater. Sci. Eng. A* **833**, 142493 (2022)
31. K.L. Johnson, *Contact Mechanics* (Cambridge University Press, Cambridge, 1985)
32. Y. Sun, S. Zheng, T. Bell, J. Smith, *Philos. Mag. Lett.* **79**, 649–658 (1999)
33. F. Lani, Q. Furnémont, T. Van Rompaey, F. Delannay, P.J. Jacques, T. Pardoen, *Acta Mater.* **55**, 3695–3705 (2007)
34. S. Shim, H. Bei, E.P. George, G.M. Pharr, *Scr. Mater.* **59**, 1095–1098 (2008)
35. B.B. He, M.X. Huang, Z.Y. Liang, A.H.W. Ngan, H.W. Luo, J. Shi, W.Q. Cao, H. Dong, *Scr. Mater.* **69**, 215–218 (2013)
36. K. Durst, B. Backes, O. Franke, M. Göken, *Acta Mater.* **54**, 2547–2555 (2006)
37. X. Ma, W. Higgins, Z. Liang, D. Zhao, G.M. Pharr, K.Y. Xie, *Proc. Natl. Acad. Sci. USA* **118**(30), e2025657118 (2021)
38. G.M. Pharr, E.G. Herbert, Y. Gao, *Annu. Rev. Mater. Res.* **40**, 271–292 (2010)
39. F. Alisafaei, C.-S. Han, N. Garg, *Int. J. Plast.* **77**, 30–53 (2016)
40. E. Bittencourt, *Int. J. Plast.* **53**, 1–16 (2014)
41. M.-Y. Seok, Y.-J. Kim, I.-C. Choi, Y. Zhao, J.-. Jang, *Int. J. Plast.* **59**, 108–118 (2014)
42. K. Danas, V.S. Deshpande, N. Fleck, *J. Mech. Phys. Solids*. **60**, 1605–1625 (2012)

43. W.W. Gerberich, J.C. Nelson, E.T. Lilleodden, P. Anderson, J.T. WYROBEK, *Acta Mater.* **44**, 3585–3598 (1996)
44. C. Tromas, J. Colin, C. Coupeau, J.C. Girard, J. Woïgard, J. Grilhé, *Eur. Phys. J. Appl. Phys.* **8**, 123–128 (1999)
45. L. Zhang, T. Ohmura, *Phys. Rev. Lett.* **112**, 145504 (2014)
46. A. Gouldstone, K.J. Van Vliet, S. Suresh, *Nature* **411**, 656 (2001)
47. K.J. Van Vliet, J. Li, T. Zhu, S. Yip, S. Suresh, *Phys. Rev. B* **67**, 104105 (2003)
48. C.A. Schuh, J.K. Mason, A.C. Lund, *Nat. Mater.* **4**, 617–621 (2005)
49. J.K. Mason, A.C. Lund, C.A. Schuh, *Phys. Rev. B* **73**, 054102 (2006)
50. Y. Sato, S. Shinzato, T. Ohmura, T. Hatano, S. Ogata, *Nat. Commun.* **11**, 4177 (2020)
51. S. Sinha, R.A. Mirshams, T. Wang, S.S. Nene, M. Frank, K. Liu, R.S. Mishra, *Sci. Rep.* **9**, 6639 (2019)
52. C.A. Schuh, *Mater. Today* **9**, 32–40 (2006)
53. Y.Z. Xia, H. Bei, Y.F. Gao, D. Catoor, E.P. George, *Mater. Sci. Eng. A* **611**, 177–187 (2014)
54. T. Chen, L. Tan, Z. Lu, H. Xu, *Acta Mater.* **138**, 83–91 (2017)
55. J.R. Trelewicz, C.A. Schuh, *Acta Mater.* **55**, 5948–5958 (2007)
56. R. Goodall, T.W. Clyne, *Acta Mater.* **54**, 5489–5499 (2006)
57. L.E. Samuels, T.O. Mulhearn, *J. Mech. Phys. Solids* **5**, 125–134 (1957)
58. T.O. Mulhearn, *J. Mech. Phys. Solids* **7**, 85–88 (1959)
59. L.F. Liu, Q.Q. Ding, Y. Zhong, J. Zou, J. Wu, Y.L. Chiu, J.X. Li, Z. Zhang, Q. Yu, Z.J. Shen, *Mater. Today* **21**, 354–361 (2018)
60. Z. Li, B. He, Q. Guo, *Scr. Mater.* **177**, 17–21 (2020)
61. B. Barkia, P. Aubry, P. Haghi-Ashtiani, T. Auger, L. Gosmain, F. Schuster, H. Maskrot, *J. Mater. Sci. Technol.* **41**, 209–218 (2020)
62. D. Tabor, *J. Inst. Metals* **79**, 1 (1951)
63. Y. Cao, Z. Xue, X. Chen, D. Raabe, *Scr. Mater.* **59**, 518–521 (2008)

Publisher's Note Springer Nature remains neutral with regard to jurisdictional claims in published maps and institutional affiliations.

Springer Nature or its licensor (e.g. a society or other partner) holds exclusive rights to this article under a publishing agreement with the author(s) or other rightsholder(s); author self-archiving of the accepted manuscript version of this article is solely governed by the terms of such publishing agreement and applicable law.